



PRIX: Learning to Plan from Raw Pixels for End-to-End Autonomous Driving

Maciej Wozniak¹, Lianhang Liu^{1,2}, Yixi Cai¹, Patric Jensfelt¹

Abstract—While end-to-end autonomous driving models show promising results, their practical deployment is often hindered by large model sizes, a reliance on expensive LiDAR sensors and computationally intensive BEV feature representations. This limits their scalability, especially for mass-market vehicles equipped only with cameras. To address these challenges, we propose PRIX (Plan from Raw pIXels). Our novel and efficient end-to-end driving architecture operates using only camera data, without explicit BEV representation and forgoing the need for LiDAR. PRIX leverages a visual feature extractor coupled with a generative planning head to predict safe trajectories from raw pixel inputs directly. A core component of our architecture is the Context-aware Recalibration Transformer (CaRT), a novel module designed to effectively enhance multi-level visual features for more robust planning. PRIX achieves SOTA performance on the NavSim-v2 and nuScenes datasets. On NavSim-v1, it also outperforms the majority of multimodal planners and other camera-only approaches on most metrics. Critically, PRIX is significantly more efficient on NavSim-v1, boasting faster inference speeds and a smaller model size. This combination of performance and efficiency makes it a practical solution for real-world deployment. Our work is open-source and the code will be available upon publication. Check our project website for more <https://maxiuw.github.io/prix>.

Index Terms—Deep Learning for Visual Perception, Visual Learning, Motion and Path Planning

I. INTRODUCTION

IN recent years, end-to-end autonomous driving has emerged as a prominent research direction, driven by its “all-in-one” training pipeline and goal-oriented output (final trajectory). End-to-end models aim to learn a direct mapping from sensor inputs to the vehicle’s trajectory through large-scale data-driven approaches. Compared with traditional modular pipelines, where perception, prediction, and planning are trained and designed, this paradigm streamlines the overall system and reduces the risk of error propagation between subsystems [1]. However, achieving robust and scalable end-to-end solutions in real-world, dynamic environments remains a major challenge.

Manuscript received: Nov 19, 2025; Revised Jan 18, 2026; Accepted March 3, 2026.

This paper was recommended for publication by Editor A. Bera upon evaluation of the Associate Editor and Reviewers’ comments. This work was supported by the Wallenberg AI, Autonomous Systems and Software Program (WASP)

¹All authors are with the Robotics Perception and Learning Department, KTH Royal Institute of Technology, Stockholm, Sweden. Corresponding Author: Yixi Cai (yixica@kth.se)

²Second Author is also with SCANIA, Stockholm, Sweden
Digital Object Identifier (DOI): see top of this page.

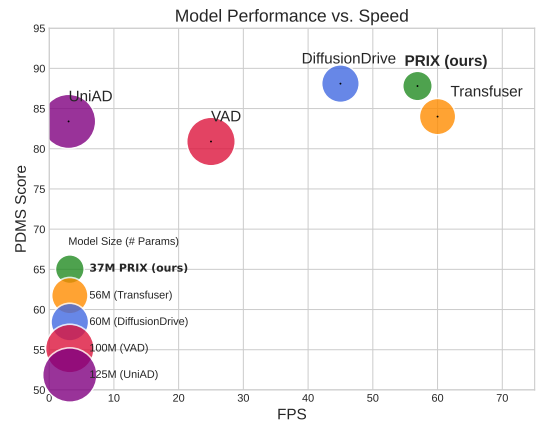


Fig. 1: Performance vs. inference speed comparing our camera-only model, **PRIX**, to leading methods on the NavSim-v1 benchmark. **PRIX** outperforms or matches the performance of multimodal methods SOTA like DiffusionDrive [2], while being significantly smaller and faster. Notably, it operates at a highly competitive framerate, falling only 3 FPS behind the fastest model, Transfuser [6], while substantially outperforming it in PDMS.

Whether using cameras, LiDAR, or both, the computational cost of feature extraction significantly constrains the resources available for increasingly complex end-to-end planning architectures. Current state-of-the-art (SOTA) end-to-end autonomous driving methods [2, 3, 4, 5] have focused on fusing multiple sensor modalities, primarily camera and LiDAR, to build a comprehensive environmental representation [2, 3, 4, 5, 6]. While effective, this reliance on expensive LiDAR sensors and computationally intensive methods limits the scalability of such systems, particularly for mass-market consumer vehicles, which are typically equipped only with cameras, limiting their applicability to vehicles with more expensive sensor suites. Moreover, all these methods depend on BEV (Bird’s-Eye View) features, which are computationally expensive, especially for the camera branch, which has to be cast to BEV, e.g., LSS-type models [7]. On the other hand, many existing camera-only end-to-end approaches suffer from significant practical limitations. Notably, leading camera-only architectures like UniAD and VAD [8, 9] are often oversized, containing over 100 million parameters. This large size makes them computationally expensive, resulting in slower inference speeds and more demanding training requirements.

While all components of end-to-end models are integral, we

argue that the primary *determinant of system performance* is the visual feature extractor. Its ability to learn task-relevant representation plays the key role in the success of the downstream planning task. However, it is also often the visual feature extractor that is driving the computational cost.

We posit that it is possible to learn rich visual representations directly from camera inputs for planning without explicitly depending on BEV representation or 3D geometry from LiDAR. Through a detailed analysis of training losses, model design, and experiments with various planning heads, we demonstrate the importance of visual features in end-to-end learning. Our focus on visual camera-only learning is motivated by recent advancements from visual foundation models and world models [10] that have proven that rich, high-fidelity 3D representations of the world can be learned directly from cameras [11, 12]. This camera-only paradigm opens the door for powerful, low-cost autonomous systems suitable for a wide range of customer-level vehicles. The autonomous driving domain is particularly well-suited for this approach; vehicles are commonly equipped with 6 to 10 cameras [13, 14, 15], making learning of spatial visual representation feasible.

Inspired by these works, we propose **Plan from Raw Pixels (PRIX)**: a novel end-to-end driving architecture that operates using only camera data and forgoes the need for LiDAR or BEV features. Our method uses a smart visual feature extractor coupled with a generative planning head to directly predict safe trajectories. We demonstrate that our approach successfully predicts future trajectories outperforming other camera-only and most of the multimodal SOTA approaches while being significantly faster and requiring less memory, as shown in Fig. 1. This makes PRIX a practical solution for real-world deployment. Our contributions are as follows:

- We introduce **PRIX**, a novel camera-only, end-to-end planner that is significantly more efficient than multimodal and previous camera-only approaches in terms of inference speed and model size.
- We propose **Context-aware Recalibration Transformer (CaRT)**, a new module designed to effectively enhance multi-level visual features for more robust planning.
- We provide a **comprehensive ablation study** that validates our architectural choices and offers insights into optimizing the trade-off between performance, speed, and model size.
- Our method achieves SOTA performance on the NavSim-v2 and nuScenes datasets, as well as most of the NavSim-v1 metrics outperforming the majority of multimodal planners and other camera-only approaches while being much smaller and faster.

II. RELATED WORK

Multimodal End-to-End Driving To achieve a comprehensive perception of the environment, many recent studies emphasize fusing data from multiple sensors like cameras and LiDAR [16]. Initial works like Transfuser [6] used a complex transformer architecture for this fusion. Building this robust world model is the foundational first step; however,

the ultimate goal is to translate this perception into safe and effective driving actions. This crucial transition from perception to planning has spurred its own wave of innovation. Early approaches like Hydra-MDP [4] discretized the planning space into sets of trajectories. To overcome the limitations of predefined anchors (pre-set potential trajectories), subsequent research has focused on generating more flexible, continuous paths. This includes diffusion models like TransDiffuser [5] or DiffusionDrive [2], which create diverse trajectories without thousands of anchors. To further reduce inference complexity, GoalFlow [3] employs a flow matching method instead of diffusion, which learns a simpler mapping from noise to the trajectory distribution.

Architectural innovations have also been key; such as DRAMA [17] that leverages the Mamba state-space model for computational efficiency or ARTEMIS [18] uses a Mixture of Experts (MoE) for adaptability in complex scenarios

An alternative paradigm is Reinforcement Learning (RL), where models like RAD [19] are trained via trial and error in photorealistic simulations built with 3D Gaussian Splatting, helping to overcome the causal confusion issues of imitation learning. Despite these advances, a critical perspective from Xu et al. [20] highlights a significant performance gap when models are applied to noisy, real-world sensor data, underscoring the importance of robust intermediate perception.

While SOTA methods demonstrate powerful capabilities, they are often complex and depend on multimodal sensors. In contrast, our proposed method is designed for simplicity, using only a single modality while achieving better or comparable performance.

Camera only End-to-End Driving End-to-end autonomous driving has evolved from camera-only systems to language-enhanced models. Early camera-only methods like UniAD [8] established unified frameworks for perception, prediction, and planning. To improve efficiency over dense BEV representations, subsequent works introduced more structured alternatives, such as the vectorized scenes in VAD [9, 21], sparse representations in Sparsedrive [22], 3D semantic Gaussians [11], or lightweight polar coordinates. Planning processes were also refined through iterative techniques in models like PPAD [23], while others focused on robustness with Gaussian processes (RoCA [24]) or precise trajectory selection (DriveSuprim [25], GTRS [26]). Efficiency has also been addressed at the input level with novel tokenization strategies [27].

More recently, Vision Language Models (VLMs) have been integrated to enhance reasoning. LeGo-Drive [28] uses language for high-level goals, while SOLVE [29] and Dif-fVLA [30] leverage VLMs for action justification and to guide planning. To manage the high computational cost, methods like DiMA [31] distill knowledge from large models into more compact planners. The capabilities of these advanced models are assessed using new evaluation frameworks like LightEMMA [32].

In contrast to many oversized and slower camera-only methods, PRIX is designed to balance high performance with computational speed, as shown in Fig. 1. As shown in Sec. IV, our model outperforms other camera-only models on available benchmarks while being much more efficient.

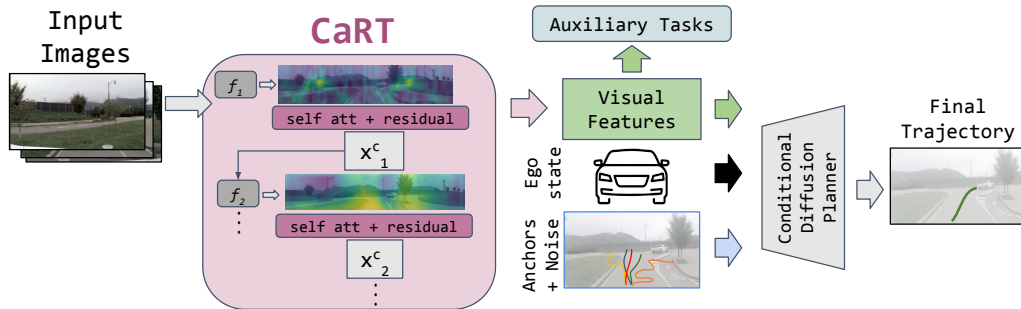


Fig. 2: **PRIX Overview**: Visual features from multi-camera images are extracted by ResNet layers (f_i) and together with self-attention and skip connections (*CaRT*, described in Sec. III-A). Next, visual features are used for auxiliary perception tasks (see Sec. III-E) and trajectory planning (see Sec. III-C).

III. METHOD

The goal of our end-to-end autonomous driving model, shown in Fig. 2, is to generate the best future trajectory of the ego-vehicle from raw camera data. We use only the current time-step camera and the ego vehicle’s status (velocity, acceleration, and navigation commands) as an input. Our model outputs: 8-waypoint trajectory over 4 sec at 2 Hz, with each waypoint defined by x, y, and heading. Camera only feature extraction, detailed in Sec. III-A, is a base for the conditional denoising diffusion planner, described in Sec. III-C. We detail and justify our design choices in Sec. III-D and the main objective and auxiliary tasks are discussed in Sec. III-E.

A. Visual Feature Extraction

The foundation of our proposed method is a lightweight, camera-only, visual feature extractor designed to derive a rich, *multi-scale representation* of the driving scene, as shown in Fig. 3. This hierarchical approach is critical for autonomous driving, a task that demands both high-level semantic understanding (e.g., an upcoming intersection) and precise low-level spatial detail (e.g., tracking the exact lane curvature).

To generate and refine these multi-scale features, we employ a ResNet as the hierarchical backbone, which naturally extracts feature maps (x_i) at distinct resolutions. However, with raw ResNet features, we face a classic dilemma: early layers capture fine spatial details but lack scene-level understanding, while deeper layers possess rich semantic context but are spatially coarse. To address this, we introduce our novel **Context-aware Recalibration Transformer (CaRT)** module inspired by previous works as SE [33] and CBAM [34].

The feature map x_i , where $i \in \{1, 2, 3, 4\}$, is first spatially standardized via adaptive average pooling to a fixed size (512 feature size in our implementation, see Sec. III-D for ablation studies). Next, features are processed by a self-attention (SA) part of a CaRT module to model long-range dependencies across the spatial domain (see Fig. 3). A single, weight-shared multi-head self-attention block is applied to each sequence of tokens (explained in Sec. III-D). For each feature level i , we compute the Query (Q_i), Key (K_i), and Value (V_i) matrices using shared linear projection matrices W_Q , W_K , and W_V : $Q_i = x_i W_Q$, $K_i = x_i W_K$, $V_i = x_i W_V$.

The output of the CaRT module is the attention A_i computed using the scaled dot-product attention $A(Q_i, K_i, V_i) =$

$\text{softmax}\left(\frac{Q_i K_i^T}{\sqrt{d_k}}\right) V_i$. A_i , which is our recalibrated feature map, is then upsampled to the original dimensions of x_i , concatenated with the original x_i feature map (extracted from ResNet) via skip connection, creating x_i^c , and fed to the next ResNet layer f_{i+1} as shown in Fig. 3.

The iterative *recalibration* process actively refines the initial feature maps from the ResNet backbone by infusing them with global semantic context learned via SA. This effectively adjusts the value and significance of the initial local features based on the newly understood global context. It is not just adding new information; it is fundamentally changing the interpretation of the existing features by infusing them with the global context of the entire scene generated by the CaRT self-attention layers. The final feature map is *Global Features*, $x_5^G \in \mathbb{R}^{B \times C_c \times H_c \times W_c}$, which encapsulates information from all levels. To synthesize the final multi-scale representation, the architecture ends in a top-down pathway, analogous to a Feature Pyramid Network (FPN). The Semantic Features are passed through a series of upsampling and 3x3 convolutional layers to restore a higher-resolution feature map, ensuring it benefits from semantic context while retaining precise spatial understanding, we refer to it as *Local Features*, $x_5^L \in \mathbb{R}^{B \times C_L \times H_L \times W_L}$.

B. From Camera Features to Trajectories Without Geometric BEV

Planning operates on two learned representations: a *Token Memory* (derived from global features x_5^G plus an ego-status token) and a *Planner Grid* (obtained by mixing this memory with local features x_5^L). The planner grid is *not* a geometric BEV; it is a learned canonical grid aligned to the ego frame through supervision. We rely on a fixed camera rig with constant view ordering and resolution.

Under this setup, camera geometry is constant and absorbed by the network parameters. Consequently, the planner grid is anchored to the ego frame solely through semantic and trajectory losses; no camera intrinsics or extrinsics are used.

The *Token Memory* is built by flattening x_5^G into $(H_c W_c)$ visual tokens and appending a status token. A learned index embedding is added to encode the view identity and the spatial slot. The resulting memory serves as Keys and Values for the transformer decoding stage, where a learned query attends to the token memory before splitting into trajectory

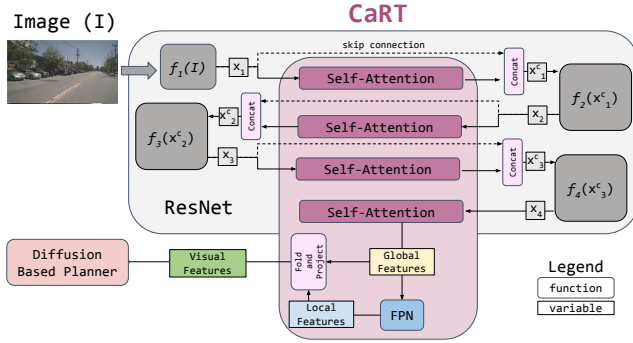


Fig. 3: Architecture of our visual feature extractor with **Context-aware Recalibration Transformer (CaRT)** module.

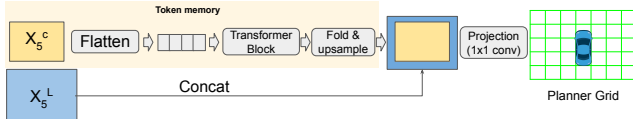


Fig. 4: Fold and Project flowchart.

and agent queries. To provide spatial structure for the grid, this same memory is “folded” back into 2D. The status token is discarded, and the remaining visual tokens are reshaped into an $H_c \times W_c$ map, upsampled to (H_L, W_L) , and concatenated with the local feature x_5^L . A point-wise projection Φ then produces the *planner grid* \mathbf{G} . The entire fold-and-project pipeline is learned, allowing supervision to stabilize \mathbf{G} as a canonical planning representation.

C. Diffusion-Based Trajectory Planner

For planning, we adopt a conditional denoising diffusion head from DiffusionDrive [2] that generates trajectories via iterative refinement (we also test different planners in Sec. IV-C, showing our method performs well with any planner). Unlike regression-based planners, this approach treats trajectory prediction as a denoising process: given noisy trajectory proposals (anchors), ego state, and visual features, the model gradually refines them into feasible plans.

The trajectory is represented as a sequence of waypoints, $\tau = (x_t, y_t)_{t=1}^{T_f}$, where T_f is the planning horizon and (x_t, y_t) is the waypoint location at future time t in the ego-vehicle’s coordinate system.

The *forward process*, q , progressively adds Gaussian noise to a clean trajectory τ^0 over n timesteps. In one step: $q(\tau^i | \tau^0) = \mathcal{N}(\tau^i; \sqrt{\bar{\alpha}^i} \tau^0, (1 - \bar{\alpha}^i) \mathbf{I})$, where i is the diffusion timestep and $\bar{\alpha}^i = \prod_{s=1}^i (1 - \beta^s)$. As $i \rightarrow n$, τ^i converges to an isotropic Gaussian. The *reverse process* learns to remove noise and recover the trajectory. We train a model, ϵ_θ , to predict the noise component ϵ at timestep i .

This process is conditioned on visual features c_{visual} , ego state c_{ego} and a set of noisy anchors. Following DiffusionDrive [2], we generate a vocabulary of trajectory anchors by performing K-Means clustering on the ground-truth trajectories of the training dataset. Each cluster centroid represents a distinct driving intention (e.g., turn left, lane keep). During training, we select the anchor closest to the ground truth and corrupt it with Gaussian noise to create c_{anch} . This “anchored”

initialization provides a strong prior, allowing the diffusion model to refine the trajectory in very few steps (e.g., $n = 2$) compared to generating from pure noise, significantly reducing inference latency.

D. Design choices and findings

Our initial design consisted of a visual feature extractor with separate SA modules in CaRT corresponding to each feature level of ResNet backbone and two-step diffusion planner. Throughout this section, we analyze our design in detailed ablation studies on Navsim-v1 and evaluate using PDMS (explained in Sec. IV) to arrive at the final configuration of our model.

a) Module Integration Strategy Our experiments show that using a CaRT module where the self-attention layers share weights across all feature scales of the backbone outperforms using separate, specialized SA for each x_i . As detailed in Tab. I, this shared-weight design not only achieves a higher score but also reduces the parameter count and increases inference speed. This indicates that the core logic of using global context to recalibrate local features is a universal principle. Forcing a single set of self-attention weights to learn this logic across different levels of feature abstraction results in a more robust and generalized representation.

TABLE I: Ablation on sharing weights in SA layers in CaRT module across different scales.

Configuration	Params ↓	PDMS ↑	FPS ↑
Separate SA	39M	87.3	54.4
Shared SA 256	33M	87.0	57.9
Shared SA 512	37M	87.8	57.0
Shared SA 768	39M	87.7	56.0

b) Anchors with end points Inspired by the concept of GoalFlow [3], in Tab. II we experimented with using the final end point as an additional conditioning signal for our diffusion head planner, aiming to help the final trajectory objective. We hypothesized that this would complement the guidance from the anchors. However, our findings indicate that the combination of anchors and end points is counterproductive and appears to confuse the planner, creating a conflict between the local, step-by-step guidance from anchors and the global pull of the final destination. As a result, this combination led to a slight degradation in performance, suggesting that anchors alone are a better approach, which we used in our model.

TABLE II: Ablation on anchors plus end points

Model	Anchors	End-Points	PDMS ↑
anchors-only	✓		87.8
end-points only		✓	83.5
anchors+end points	✓	✓	85.9

c) Overall Impact of CaRT To quantify the contribution of the CaRT module and justify its computational cost, we created a baseline version of PRIX without it. The residual connection still exists but processes features that are only downsampled and upsampled, without any transformer-based processing. In Tab. III we show that removing the module reduces parameters and increases speed but model performance drastically drops.

Therefore, we included the CaRT module in our final model, as it provides a significant performance boost while remaining highly efficient.

TABLE III: Ablation on the existence of the CaRT module.

Configuration	Parameters↓	PDMS ↑	FPS↑
PRIX (with CaRT)	37M	87.8	57.0
PRIX (no CaRT)	20M	76.4	70.9

d) Diffusion steps We experimented with various truncated diffusion time steps, specifically 2-50 and evaluated performance using the PDMS shown in Fig. 5. The results showed that performance degrades when the number of diffusion steps increases. Such over-smoothing diminishes the quality of the final predictions, reflected in the notable drop in PDMS at higher step counts; thus, we opt for 2 steps.

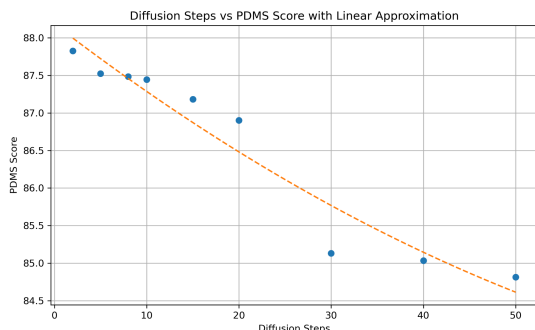


Fig. 5: Diffusion steps vs performance on Navsim-v1.

E. Training Objectives and Auxiliary Tasks

Relying solely on a trajectory imitation loss, as shown in Tab. VII and other works [2, 6, 9], is *insufficient* for an end-to-end model to learn the rich representations needed for robust autonomous driving. To address this, we employ a multi-task learning paradigm. By adding auxiliary tasks, we introduce a powerful inductive bias that compels our camera-only feature extractor to learn a more structured, semantically meaningful world representation specialized for autonomous driving, ultimately leading to better planning. Our total loss is a weighted sum of the primary planning task and auxiliary objectives:

$$\mathcal{L} = \lambda_{\text{plan}}\mathcal{L}_{\text{plan}} + \lambda_{\text{det}}\mathcal{L}_{\text{det}} + \lambda_{\text{sem}}\mathcal{L}_{\text{sem}}, \quad (1)$$

where λ terms are the corresponding loss weights.

Primary Planning Loss ($\mathcal{L}_{\text{plan}}$) Our model learns the ego-vehicle’s future path by minimizing the L1 distance between the predicted waypoints $\hat{\mathbf{p}}_{1:T}$ and the ground-truth trajectory $\mathbf{p}_{1:T}$. This loss, defined as $\mathcal{L}_{\text{plan}} = \frac{1}{T} \sum_{t=1}^T \|\hat{\mathbf{p}}_t - \mathbf{p}_t\|_1$, optimizes the final trajectory. **Auxiliary Task: Object Detection (\mathcal{L}_{det})** Safe navigation requires awareness of other road users. We add an auxiliary objective to localize traffic participants like vehicles and pedestrians. This ensures the model’s internal representations are sensitive to dynamic agents that influence planning. The detection loss, $\mathcal{L}_{\text{det}} = \lambda_{\text{cls}}\mathcal{L}_{\text{cls}} + \lambda_{\text{reg}}\mathcal{L}_{\text{reg}}$, combines a focal loss for classification and an L1 loss for 3D bounding box regression. **Auxiliary Task: Semantic Consistency (\mathcal{L}_{sem})** To ensure the model understands the static

driving environment, we introduce a semantic consistency loss. This provides dense, pixel-level supervision, compelling the feature extractor to learn the scene’s structure, such as drivable areas and lane boundaries. We apply a pixel-wise cross-entropy (CE) loss, $\mathcal{L}_{\text{sem}} = \text{CE}(\hat{\mathbf{S}}, \mathbf{S})$, between the predicted $\hat{\mathbf{S}}$ and ground-truth \mathbf{S} semantic maps. This contextual understanding enables more feasible and appropriate trajectories.

IV. EXPERIMENTS

In this section, we benchmark our method against other SOTA approaches on various datasets. When reporting baseline results, we use the scores reported by the authors, unless otherwise indicated.

A. Data and metrics

NavSim-v1 [14] is a benchmark for evaluating autonomous driving agents using a non-reactive simulation where an agent plans a trajectory from initial sensor data. This approach avoids re-rendering while still enabling detailed, simulation-based analysis of the maneuver’s safety and quality. Evaluation is based on the PDMS, which aggregates several metrics. It penalizes safety failures while rewarding driving performance, calculated as:

$$\text{PDMS} = \underbrace{\prod_{m \in \{\text{NC, DAC}\}} \text{score}_m}_{\text{penalties}} \times \underbrace{\frac{\sum_{w \in \{\text{EP, TTC, C}\}} \text{weight}_w \times \text{score}_w}{\sum_{w \in \{\text{EP, TTC, C}\}} \text{weight}_w}}_{\text{weighted average}}, \quad (2)$$

where penalties come from collisions (NC) and staying in the drivable area (DAC) with a weighted average of scores for progress (EP), time-to-collision (TTC), and comfort (C).

NavSim-v2 [15] introduces *pseudo-simulation*. A planned trajectory is executed in a simulation with reactive traffic, and performance is measured by an Extended PDM Score (EPDMS). Note, NavSim-v2 is a very recent dataset and only a few approaches have been tested or adopted to it (most of them still under review).

$$\text{EPDMS} = \underbrace{\prod_{m \in M_{\text{pen}}} \text{filter}_m(\text{agent, human})}_{\text{penalty terms}} \cdot \underbrace{\frac{\sum_{m \in M_{\text{avg}}} w_m \cdot \text{filter}_m(\text{agent, human})}{\sum_{m \in M_{\text{avg}}} w_m}}_{\text{weighted average terms}} \quad (3)$$

For nuScenes [13], we follow SparseDrive [22]: stage 1 for 100 epochs followed by fine-tune stage 2 for 10 epochs using stage 1 weights. The nuScenes trajectory prediction [13] benchmark challenge is a popular and rich resource, where we compare our performance with a larger range of camera-only methods. Following previous works [2, 9], we reported average L2 error and collision rate at 3.0s horizon for a fair comparison. We compute the L2 error between the planned trajectory and the human driving trajectory, and evaluate how often we would collide with other agents on the road.

We train on a cluster with eight NVIDIA A100 (40GB) GPUs using a per-GPU batch size of 64. For inference benchmarking (Table IV), we utilize a single NVIDIA RTX 3090 (24GB) GPU. To strictly simulate real-time deployment, all reported speeds use a batch size of 1 and mixed precision

TABLE IV: Performance of different models on **Navsim-v1**. The up arrow (\uparrow) indicates that **higher values are better**. Best results are in **bold**, and second best are underlined. C&L refers to Camera and LiDAR. \dagger Default GoalFlow uses V2-99, but they also reported Resnet34. We were only able to experiment with the inference speed of the models that released their code.

Method	Conference	Input	# frames	Backbone	NC \uparrow	DAC \uparrow	TTC \uparrow	Comf. \uparrow	EP \uparrow	PDMS \uparrow	FPS \uparrow
VADv2 [21]	arXiv24	Camera	4	Resnet34	97.2	89.1	91.6	100	76.0	80.9	25
Hydra-MDP [4]	CVPRW24	C & L	4	Resnet34	97.9	91.7	92.9	100	77.6	83.0	—
UniAD [8]	CVPR23	Camera	≥ 2	Resnet34	97.8	91.9	92.9	100	78.8	83.4	3
PARA-Drive [35]	CVPR24	Camera	2	Resnet34	97.9	92.4	93.0	99.8	79.3	84.0	—
Hydra-MDP++ [36]	CVPRW25	Camera	2	Resnet34	97.6	96.0	93.1	100	<u>80.4</u>	86.6	—
Transfuser [6]	TPAMI22	C & L	1	Resnet34	97.7	92.8	92.8	100	79.2	84.0	60
GoalFlow † [3]	CVPR25	C & L	1	Resnet34	98.3	93.8	<u>94.3</u>	100	79.8	85.7	—
DiffusionDrive [2]	CVPR25	C & L	1	Resnet34	<u>98.2</u>	<u>96.2</u>	94.7	100	82.2	88.1	45
PRIX (ours)	RAL26	Camera	1	Resnet34	98.1	96.3	94.1	100	82.3	<u>87.8</u>	<u>57</u>

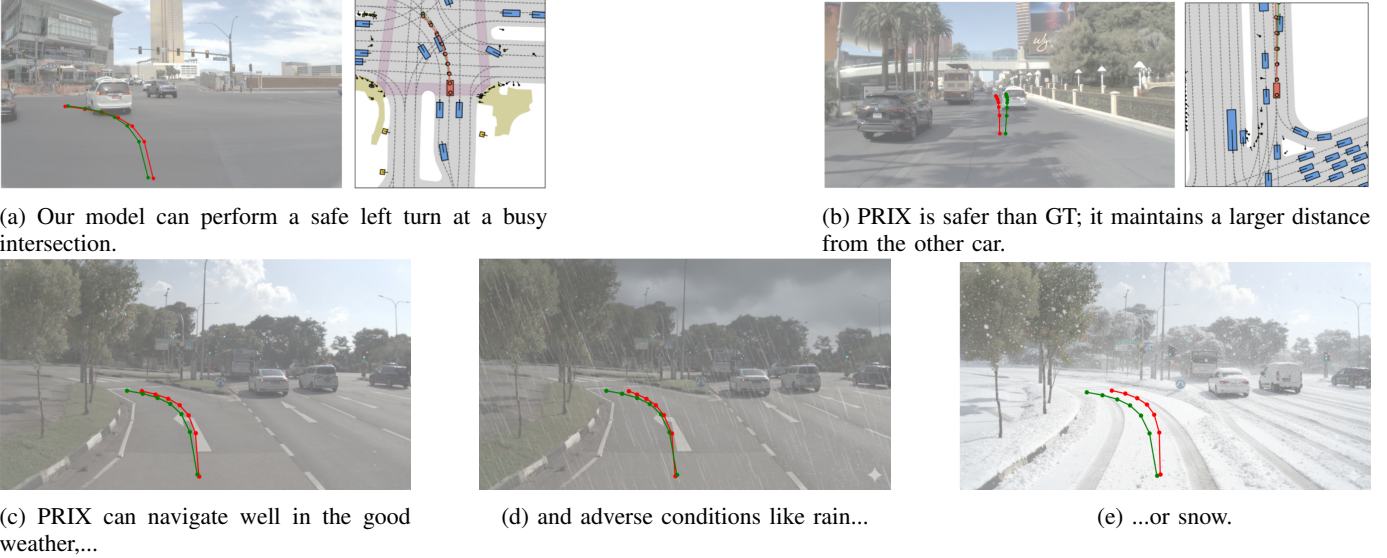


Fig. 6: Qualitative trajectory predictions from PRIX. In some cases, like **6b**, our predictions are safer than the GT.

TABLE V: Performance comparison of different driving models for **Navsim-v2**. The up arrow (\uparrow) indicates that **higher values are better**. Best results are in **bold**, and second best are underlined. All the methods are camera-only.

Method	Backbone	NC \uparrow	DAC \uparrow	DDC \uparrow	TL \uparrow	EP \uparrow	TTC \uparrow	LK \uparrow	HC \uparrow	EC \uparrow	EPDMS \uparrow
Human Agent	—	100	100	99.8	100	87.4	100	100	98.1	90.1	90.3
Ego Status MLP	—	93.1	77.9	92.7	99.6	86.0	91.5	89.4	98.3	85.4	64.0
Transfuser [6]	Resnet34	96.9	89.9	97.8	<u>99.7</u>	87.1	95.4	92.7	98.3	<u>87.2</u>	76.7
HydraMDP++ [36]	Resnet34	97.2	97.5	<u>99.4</u>	99.6	83.1	<u>96.5</u>	94.4	98.2	70.9	81.4
DriveSuprim [25]	Resnet34	<u>97.5</u>	<u>96.5</u>	<u>99.4</u>	99.6	88.4	<u>96.6</u>	<u>95.5</u>	98.3	77.0	<u>83.1</u>
PRIX (ours)	Resnet34	98.0	95.6	99.5	99.8	<u>87.4</u>	97.2	97.1	98.3	87.6	84.2

(FP16), encompassing the full forward pass from input tensors to final trajectory generation. We further verified these latency figures on an NVIDIA A100, observing consistent performance (variance within $\pm 0.5\%$ of the speed) on inference. On Navsim [14], we train for 100 epochs. Optimization uses AdamW with an initial learning rate of 10^{-5} , weight decay 10^{-3} , $(\beta_1, \beta_2) = (0.9, 0.999)$, and $\epsilon = 10^{-8}$. The learning rate follows a MultiStepLR schedule with milestones at epoch 70 and a decay factor $\gamma = 0.1$. We apply a parameter-wise LR multiplier of 0.5 to the image encoder relative to the rest of the model. All training configurations, additional experiments, and qualitative results can be found on our [project website](#).

B. Benchmarks

By leading in the most scores and key safety metrics on Navsim-v1, Navsim-v2 and nuScenes (Tabs. IV and V) against the majority of the models, PRIX is an effective, well-balanced camera-only solution for autonomous navigation; qualitative examples are in Fig. 1 (and more on the project website).

On Navsim-v1, PRIX ranks first among camera-only methods with a PDMS of 87.8; only the multimodal DiffusionDrive [2] scores higher overall. Notably, PRIX surpasses other models that use Camera+LiDAR inputs, such as GoalFlow [3], and attains top ranks on critical safety and performance metrics, even with adverse weather, see Fig. 6 (check our project website for more qualitative results). Importantly, PRIX achieves this while operating at 57 FPS, far above most

TABLE VI: Performance comparison of different driving models for **nuScenes**. The down arrow (\downarrow) indicates that **lower values are better**. Best results are in **bold**, and second best are underlined.

Method	Input	Backbone	L2 (m) \downarrow				Collision Rate (%) \downarrow				FPS \uparrow
			1s	2s	3s	Avg.	1s	2s	3s	Avg.	
ST-P3 [37]	Camera	EffNet-b4	1.33	2.11	2.90	2.11	0.23	0.62	1.27	0.71	1.6
UniAD [8]	Camera	ResNet-101	0.45	0.70	1.04	0.73	0.62	0.58	0.63	0.61	1.8
OccNet [38]	Camera	ResNet-50	1.29	2.13	2.99	2.14	0.21	0.59	1.37	0.72	2.6
VAD [9]	Camera	ResNet-50	0.41	0.70	1.05	0.72	0.07	0.17	0.41	0.22	4.5
SparseDrive [22]	Camera	ResNet-50	<u>0.29</u>	<u>0.58</u>	<u>0.96</u>	<u>0.61</u>	<u>0.01</u>	<u>0.05</u>	0.18	<u>0.08</u>	<u>9.0</u>
DiffusionDrive* ¹ [2]	Camera	ResNet-50	0.31	0.62	1.03	0.65	0.03	0.06	<u>0.19</u>	0.09	8.2
PRIX (ours)	Camera	ResNet-50	0.26	0.53	0.93	0.57	0.00	0.04	0.18	0.07	11.2

*¹ We and other researchers were not able to reproduce results reported on nuScenes. We included the results we obtained. <https://github.com/hustvl/DiffusionDrive/issues/57> as well as `issues/45`. We still outperform the reported results [2].

baselines. Unlike HydraMDP++ [36] (2 frames), UniAD [8] (≥ 2 frames), or VAD [21] (4 frames), PRIX uses only a current frame while remaining competitive or superior across safety measures. As with all approaches, ego state information (velocity, acceleration) is provided; however, PRIX extracts more from less input, demonstrating that a camera-only, 1-frame design can still outperform methods with richer temporal or multimodal inputs. On the newer Navsim-v2 benchmark, PRIX again leads with an EPDM of 84.2 and shows robust EC performance, outperforming HydraMDP++.

PRIX also achieves SOTA performance on the nuScenes trajectory prediction challenge, outperforming all existing camera-based baselines, shown in Tab. VI. In terms of average L2 error across 1s to 3s horizons, PRIX achieves the lowest value of 0.57m, surpassing the previously best DiffusionDrive (0.65 m) and SparseDrive (0.61 m). Moreover, PRIX yields the lowest collision rate at 0.07%, with a 0.00% collision rate at 1 second, indicating strong short-term safety. Notably, PRIX also operates at the highest inference speed (11.2 FPS), demonstrating that our model offers a superior balance of accuracy, safety, and efficiency.

C. Ablations

We further ablate different components of our model after initial design analysis in Sec. III-D. All ablations are done on Navsim-v1. More ablations can be found on our [project website](#). **Loss influence:** We demonstrate the progressive benefit of each auxiliary loss. We show that using only planning as supervision is not enough. The baseline model, using only the planning loss ($\mathcal{L}_{\text{plan}}$), scores 70.4 on PDMS. Adding tasks responsible for environment understanding, such as agent detection and classification, plus semantic segmentation, successively boosts the score as shown in Tab. VII. That confirms that the planner’s performance is directly coupled with the quality of the features, which learn a semantically rich representation of the scene through these auxiliary tasks.

TABLE VII: Contribution of each loss component.

Exp. #	$\mathcal{L}_{\text{plan}}$	\mathcal{L}_{box}	\mathcal{L}_{sem}	\mathcal{L}_{cls}	PDMS \uparrow
1	✓				70.4
2	✓	✓			82.3
2	✓		✓		85.7
3	✓	✓	✓		86.9
4 (Full)	✓	✓	✓	✓	87.8

Different Planners: Results in Tab. VIII affirm our core hypothesis that visual feature extractor is the most critical

component. While our top-performing diffusion planner is also the slowest at 57.0 FPS, a simple MLP head is highly competitive. This strong performance from a minimal planner proves the richness of the learned visual representation. A clear trade-off exists: for applications requiring higher speed, the diffusion head can be swapped for much faster alternatives, like the MLP or the second-best LSTM, with only a minor compromise in accuracy. This confirms that foundational heavy lifting is handled by the visual encoder.

TABLE VIII: Planners comparison, all models use ResNet34.

Model	Planner	PDMS \uparrow	Params \downarrow	FPS \uparrow
PRIX (baseline)	Diffusion	87.8	37M	57.0
PRIX-mlp	MLP	85.1	33M	65.3
PRIX-t	Transformer	85.4	35M	62.8
PRIX-ls	LSTM	86.7	34M	63.4

Limitation and future work While PRIX achieves great performance on every popular end-to-end driving benchmark, its camera-only nature makes it vulnerable to adverse weather, occlusions, and sensor failure or decalibration. Future work can enhance robustness through two main avenues. First, self-supervised pre-training on large, unlabeled datasets could help the backbone learn more resilient features [39, 40]. Second, incorporating control [41] or rule-based approaches [42] could better manage uncertainties and improve safety in challenging scenarios. While PRIX performs well on adverse weather or partially missing data, it does not generalize between different sensor setups and would have to be retrain for each. Generalization is something we will explore in future work. Additionally, recent works argue that good representation and planning can be learnt and with supervision based on future frame prediction [43], which is worth trying in the future.

V. CONCLUSIONS

We introduce PRIX, an efficient camera-only driving model that outperforms other published vision-based methods and rivals SOTA multimodal systems. While LiDAR remains important for robustness, we show that high performance is achievable with vision alone, demonstrating that leveraging rich camera features for planning is a viable alternative to BEV and multimodal approaches, and establishing a new benchmark for efficient, vision-based autonomous driving.

REFERENCES

- [1] L. Chen, P. Wu, K. Chitta, B. Jaeger, A. Geiger, and H. Li, “End-to-end autonomous driving: Challenges and frontiers,” *TPAMI*, 2024. 1
- [2] B. Liao, S. Chen, H. Yin, B. Jiang, C. Wang, S. Yan, X. Zhang, X. Li, Y. Zhang, Q. Zhang *et al.*, “Diffusiondrive: Truncated diffusion model for end-to-end autonomous driving,” in *CVPR*, 2025, pp. 12 037–12 047. 1, 2, 4, 5, 6, 7
- [3] Z. Xing, X. Zhang, Y. Hu, B. Jiang, T. He, Q. Zhang, X. Long, and W. Yin, “Goalflow: Goal-driven flow matching for multimodal trajectories generation in end-to-end autonomous driving,” in *CVPR*, 2025, pp. 1602–1611. 1, 2, 4, 6
- [4] Z. Li, K. Li, S. Wang, S. Lan, Z. Yu, Y. Ji, Z. Li, Z. Zhu, J. Kautz, Z. Wu *et al.*, “Hydra-mdp: End-to-end multimodal planning with multi-target hydra-distillation,” *arXiv preprint arXiv:2406.06978*, 2024. 1, 2, 6
- [5] X. Jiang, Y. Ma, P. Li, L. Xu, X. Wen, K. Zhan, Z. Xia, P. Jia, X. Lang, and S. Sun, “Transdiffuser: End-to-end trajectory generation with decorrelated multi-modal representation for autonomous driving,” *arXiv preprint arXiv:2505.09315*, 2025. 1, 2
- [6] K. Chitta, A. Prakash, B. Jaeger, Z. Yu, K. Renz, and A. Geiger, “Transfuser: Imitation with transformer-based sensor fusion for autonomous driving,” *TPAMI*, vol. 45, no. 11, pp. 12 878–12 895, 2022. 1, 2, 5, 6
- [7] J. Philion and S. Fidler, “Lift, splat, shoot: Encoding images from arbitrary camera rigs by implicitly unprojecting to 3d,” in *ECCV*. Springer, 2020, pp. 194–210. 1
- [8] Y. Hu, J. Yang, L. Chen, K. Li, C. Sima, X. Zhu, S. Chai, S. Du, T. Lin, W. Wang *et al.*, “Planning-oriented autonomous driving,” in *CVPR*, 2023, pp. 17 853–17 862. 1, 2, 6, 7
- [9] B. Jiang, S. Chen, Q. Xu, B. Liao, J. Chen, H. Zhou, Q. Zhang, W. Liu, C. Huang, and X. Wang, “Vad: Vectorized scene representation for efficient autonomous driving,” in *ICCV*, 2023, pp. 8340–8350. 1, 2, 5, 7
- [10] A. Bar, G. Zhou, D. Tran, T. Darrell, and Y. LeCun, “Navigation world models,” in *CVPR*, 2025, pp. 15 791–15 801. 2
- [11] G. Hess, C. Lindström, M. Fatemi, C. Petersson, and L. Svensson, “Splatad: Real-time lidar and camera rendering with 3d gaussian splatting for autonomous driving,” in *CVPR*, 2025, pp. 11 982–11 992. 2
- [12] A. Tonderski, C. Lindström, G. Hess, W. Ljungbergh, L. Svensson, and C. Petersson, “Neurad: Neural rendering for autonomous driving,” in *CVPR*, 2024, pp. 14 895–14 904. 2
- [13] H. Caesar, V. Bankiti, A. H. Lang, S. Vora, V. E. Liong, Q. Xu, A. Krishnan, Y. Pan, G. Baldan, and O. Beijbom, “nuscenes: A multimodal dataset for autonomous driving,” in *CVPR*, 2020, pp. 11 621–11 631. 2, 5
- [14] D. Dauner, M. Hallgarten, T. Li, X. Weng, Z. Huang, Z. Yang, H. Li, I. Gilitschenski, B. Ivanovic, M. Pavone, A. Geiger, and K. Chitta, “Navsim: Data-driven non-reactive autonomous vehicle simulation and benchmarking,” in *NeurIPS*, 2024. 2, 5, 6
- [15] W. Cao, M. Hallgarten, T. Li, D. Dauner, X. Gu, C. Wang, Y. Miron, M. Aiello, H. Li, I. Gilitschenski, B. Ivanovic, M. Pavone, A. Geiger, and K. Chitta, “Pseudo-simulation for autonomous driving,” *CoRL*, 2025. 2, 5
- [16] M. K. Wozniak, V. Kärefjård, M. Thiel, and P. Jensfelt, “Toward a robust sensor fusion step for 3d object detection on corrupted data,” *RA-L*, vol. 8, no. 11, pp. 7018–7025, 2023. 2
- [17] C. Yuan, Z. Zhang, J. Sun, S. Sun, Z. Huang, C. D. W. Lee, D. Li, Y. Han, A. Wong, K. P. Tee *et al.*, “Drama: An efficient end-to-end motion planner for autonomous driving with mamba,” *arXiv preprint arXiv:2408.03601*, 2024. 2
- [18] R. Feng, N. Xi, D. Chu, R. Wang, Z. Deng, A. Wang, L. Lu, J. Wang, and Y. Huang, “Artemis: Autoregressive end-to-end trajectory planning with mixture of experts for autonomous driving,” *arXiv preprint arXiv:2504.19580*, 2025. 2
- [19] H. Gao, S. Chen, B. Jiang, B. Liao, Y. Shi, X. Guo, Y. Pu, H. Yin, X. Li, X. Zhang *et al.*, “Rad: Training an end-to-end driving policy via large-scale 3dgs-based reinforcement learning,” *arXiv preprint arXiv:2502.13144*, 2025. 2
- [20] Y. Xu, L. Chambon, É. Zablocki, M. Chen, A. Alahi, M. Cord, and P. Pérez, “Towards motion forecasting with real-world perception inputs: Are end-to-end approaches competitive?” in *ICRA*. IEEE, 2024, pp. 18 428–18 435. 2
- [21] S. Chen, B. Jiang, H. Gao, B. Liao, Q. Xu, Q. Zhang, C. Huang, W. Liu, and X. Wang, “Vadv2: End-to-end vectorized autonomous driving via probabilistic planning,” *arXiv preprint arXiv:2402.13243*, 2024. 2, 6, 7
- [22] W. Sun, X. Lin, Y. Shi, C. Zhang, H. Wu, and S. Zheng, “Sparsedrive: End-to-end autonomous driving via sparse scene representation,” *ICRA*, 2025. 2, 5, 7
- [23] Z. Chen, M. Ye, S. Xu, T. Cao, and Q. Chen, “Ppad: Iterative interactions of prediction and planning for end-to-end autonomous driving,” in *ECCV*. Springer, 2024, pp. 239–256. 2
- [24] R. Yasarla, S. Han, H.-P. Cheng, L. Liu, S. Mahajan, A. Bhattacharyya, Y. Shi, R. Garrepalli, H. Cai, and F. Porikli, “Roca: Robust cross-domain end-to-end autonomous driving,” *arXiv preprint arXiv:2506.10145*, 2025. 2
- [25] W. Yao, Z. Li, S. Lan, Z. Wang, X. Sun, J. M. Alvarez, and Z. Wu, “Drivesuprim: Towards precise trajectory selection for end-to-end planning,” *arXiv preprint arXiv:2506.06659*, 2025. 2, 6
- [26] Z. Li, W. Yao, Z. Wang, X. Sun, J. Chen, N. Chang, M. Shen, Z. Wu, S. Lan, and J. M. Alvarez, “Generalized trajectory scoring for end-to-end multimodal planning,” *arXiv preprint arXiv:2506.06664*, 2025. 2
- [27] B. Ivanovic, C. Saltori, Y. You, Y. Wang, W. Luo, and M. Pavone, “Efficient multi-camera tokenization with triplanes for end-to-end driving,” *arXiv preprint arXiv:2506.12251*, 2025. 2
- [28] P. Paul, A. Garg, T. Choudhary, A. K. Singh, and K. M. Krishna, “Lego-drive: Language-enhanced goal-oriented closed-loop end-to-end autonomous driving,” in *iROS*. IEEE, 2024, pp. 10 020–10 026. 2
- [29] X. Chen, L. Huang, T. Ma, R. Fang, S. Shi, and H. Li, “Solve: Synergy of language-vision and end-to-end networks for autonomous driving,” in *CVPR*, 2025, pp. 12 068–12 077. 2
- [30] A. Jiang, Y. Gao, Z. Sun, Y. Wang, J. Wang, J. Chai, Q. Cao, Y. Heng, H. Jiang, Z. Zhang *et al.*, “Diffvla: Vision-language guided diffusion planning for autonomous driving,” *arXiv preprint arXiv:2505.19381*, 2025. 2
- [31] D. Hegde, R. Yasarla, H. Cai, S. Han, A. Bhattacharyya, S. Mahajan, L. Liu, R. Garrepalli, V. M. Patel, and F. Porikli, “Distilling multi-modal large language models for autonomous driving,” *CVPR*, 2025. 2
- [32] Z. Qiao, H. Li, Z. Cao, and H. X. Liu, “Lightemma: Lightweight end-to-end multimodal model for autonomous driving,” *arXiv preprint arXiv:2505.00284*, 2025. 2
- [33] J. Hu, L. Shen, and G. Sun, “Squeeze-and-excitation networks,” in *Proceedings of the IEEE conference on computer vision and pattern recognition*, 2018, pp. 7132–7141. 3
- [34] S. Woo, J. Park, J.-Y. Lee, and I. S. Kweon, “Cbam: Convolutional block attention module,” in *Proceedings of the European conference on computer vision (ECCV)*, 2018, pp. 3–19. 3
- [35] X. Weng, B. Ivanovic, Y. Wang, Y. Wang, and M. Pavone, “Para-drive: Parallelized architecture for real-time autonomous driving,” in *CVPR*, 2024, pp. 15 449–15 458. 6
- [36] K. Li, Z. Li, S. Lan, J. Liu, Y. Xie, Z. Wu, Z. Yu, J. M. Alvarez *et al.*, “Hydra-mdp++: Advancing end-to-end driving via hydra-distillation with expert-guided decision analysis,” *CVPR*, 2025. 6, 7
- [37] S. Hu, L. Chen, P. Wu, H. Li, J. Yan, and D. Tao, “St-p3: End-to-end vision-based autonomous driving via spatial-temporal feature learning,” in *ECCV*, 2022. 7
- [38] H. Liu, Y. Chen, H. Wang, Z. Yang, T. Li, J. Zeng, L. Chen, H. Li, and L. Wang, “Fully sparse 3d occupancy prediction,” pp. 18 428–18 435, 2024. 7
- [39] Y. Liu, L. Kong, J. Cen, R. Chen, W. Zhang, L. Pan, K. Chen, and Z. Liu, “Segment any point cloud sequences by distilling vision foundation models,” *NeurIPS*, vol. 36, 2024. 7
- [40] H. Govindarajan, M. K. Wozniak, M. Klingner, C. Maurice, B. R. Kiran, and S. Yogamani, “Cleverdistiller: Simple and spatially consistent cross-modal distillation,” *BMVC*, 2025. 7
- [41] T. Nyberg, C. Pek, L. Dal Col, C. Norén, and J. Tumova, “Risk-aware motion planning for autonomous vehicles with safety specifications,” in *IV*. IEEE, 2021, pp. 1016–1023. 7
- [42] Y. Zheng, R. Liang, K. Zheng, J. Zheng, L. Mao, J. Li, W. Gu, R. Ai, S. E. Li, X. Zhan *et al.*, “Diffusion-based planning for autonomous driving with flexible guidance,” *ICLR*, 2025. 7
- [43] P. Li and D. Cui, “Navigation-guided sparse scene representation for end-to-end autonomous driving,” *ICLR*, 2025. 7
- [44] D. Dan, “Formula 1 icons,” in <https://www.flaticon.com/free-icons/formula-1>. Flaticon.